

Superresolving, artifact-free optical coherence tomography with deconvolution-random phase modulation

linbo liu (✉ liulinbo@ntu.edu.sg)

Nanyang Technological University <https://orcid.org/0000-0001-6691-9253>

Xin Ge

Nanyang Technological University

Si chen

Nanyang Technological University

lin kan

Nanyang Technological University

guangming ni

University of Electronic Science and Technology of China

en bo

Nanyang Technological University

lulu wang

Nanyang Technological University

Research

Keywords:

Posted Date: April 25th, 2022

DOI: <https://doi.org/10.21203/rs.3.rs-1553887/v1>

License:   This work is licensed under a Creative Commons Attribution 4.0 International License.

[Read Full License](#)

Abstract

Deconvolution is widely used to improve resolution in microscopy. Unfortunately, deconvolution in optical coherence tomography (OCT) is sensitive to noise which inherently results in additive artifacts. These artifacts severely impair the fidelity of deconvolved images and limit its use in OCT imaging. Here we propose a framework that encodes numerical random phase masks in the Fourier space of a deconvolved OCT image, to produce a sub-resolution image with the artifacts removed. The optimized joint operation of an iterative Richardson-Lucy deconvolution and a numerical synthesis of random phase masks (RPM), termed as Deconv-RPM, enables a 2.7-fold enhancement in both transverse and axial resolutions. We demonstrate that the Deconv-RPM method allows imaging previously unresolved cellular-level details in the human labial mucosa *in vivo* with significantly improved clarity.

Introduction:

Optical coherence tomography (OCT) is a powerful technique that provides non-invasive images with micrometer resolution and millimeter depth. To assess the tissue microstructures at the cellular and subcellular level, advancements [1–5] have been made to improve spatial resolutions and image contrast. However, high-resolution OCT images often suffer from broaden or distorted point spread function (PSF) due to inherent trade-off between resolution and depth-of-focus, artifacts resulting from strong scattering, deficiencies of optical components, speckle noise caused by a coherent light source, and imaging system's noise. Without introducing more optical components, many software-based approaches have been harnessed to recover the degraded OCT images by deterministic models [6, 7] or a class of evaluation metrics [8–10]. Even that, breaking the resolution limit in high-resolution OCT images remains a challenge.

One promising super-resolution algorithm is deconvolution, which has been extensively used in the fluorescence microscopy. Many attempts have also been made in the OCT images for the mitigation of transverse and axial resolution blurring with respect to depth [11–17]. For example, deconvolution has shown the potential for super-resolution in the sparse scatterers [13]. However, when amplitude-based data is used to invert a coherent process, the image quality will be inevitably deteriorated as the operation creates sidelobes from the noise in the image around the scatterers. This drawback impedes the application of deconvolution in OCT imaging [18]. Here, we describe a post-processing algorithm Deconv-RPM, in which the Fourier or pupil plane of a deconvolved frame is separately multiplied with multiple random phase marks before the products are inverse Fourier transformed to the image plane and summed together. Random phase masks (RPM) are employed to remove the artifacts while preserving the superresolved features with deconvolution. With an analogous idea, numerical random masks methods have also been applied to digital holography for image denoising [19–21].

Transverse and axial resolutions are separable in OCT systems, where the axial resolution is governed by the central wavelength and the bandwidth of the detected light while the transverse resolution is limited by the effective numerical aperture. With a separable one-dimensional (1-D) scheme, each depth slice or

A-line of an OCT frame is deconvolved by the unregularized Richardson-Lucy algorithm. While some of the regularization constraints such as Tikhonov-Miller regularization [22] and Total Variation regularization [23] have been used to suppress noise amplification, they typically call for some prior knowledge on the measured data and have a drawback of either smooth edges or a contrast loss in the image restoration. Our approach was validated experimentally where the transverse and the axial resolution are improved 2.7-fold and 2.7-fold in the confocal region, respectively. In a turbid sample such as human labial mucosa, the unprecedented performance by Deconv-RPM was demonstrated in cross-sectional or volumetric imaging compared to the unprocessed images. Deconv-RPM was used to extract scattering signals from nonkeratinized epithelial cells and blood cells *in vivo* using normal and high-speed line scan cameras, respectively. Finally, we presented an intuitive interpretation of the effects of Deconv-RPM through simulation tests. This robust and reliable method is expected to break new ground for OCT in biomedical applications.

Method (Principle Of Deconv-rpm):

In this section, we elaborate on the Deconv-RPM method that is schematically illustrated in Fig. 1. For coherent imaging, image formation of one B-scan in OCT can be deimages are averaged, scribed as a convolution of the electric field of the original undistorted sample object $u_{obj}(x, z)$ and the 2-D PSF $h(x, z)$ followed by adding noise n ,

$$u_{img}(x, z) = u_{obj}(x, z) \otimes h(x, z) + n$$

1

The backscattered magnitude of the conventional OCT frame $|u_{img}(x, z)|$ is obtained by the Fourier transform of the raw interferogram in k_z -space. As demonstrated, the convolution kernels can be approximated by absolute values instead of the complex values [13]. The combined PSF $h(x, z)$ is the product of the individual PSF $h(r)$, can be approximated by,

$$h(r) = \exp(-r^2 / w_r^2)$$

2

where the pixel index r represents the coordinate (x, z) or y for 3D z-stacks, w_r is related to the full width at half-maximum (FWHM) Δr of $h(r)$ according to $\Delta r = 2\sqrt{\ln 2} w_r$. Shown in the flowchart, the Deconv-RPM method mainly comprises two processing steps, where physically breaking the resolution limit with deconvolution and improving the image quality with random phase masks. In step 1, Lucy-Richardson deconvolution algorithm is implemented on one B-scan $|U_{img}(r)|$, performed by the built-in MATLAB function [deconvlucy ()],

$$o_{t+1}(r) = o_t(r) \cdot \left(\frac{|u_{img}(r)|}{o_t(r) \otimes \left| \hat{h}(r) \right|} \otimes \left| \hat{h}^T(r) \right| \right)$$

3

where $o_t(r)$ is the estimated object image after t -th iteration. $\left| \hat{h}(r) \right|$ is the estimated 1-D absolute value

of the PSF and $\left| \hat{h}^T(r) \right|$ is its transposed matrix. Typically, $\left| \hat{h}(r) \right|$ is set as space-invariant in Lucy-

Richardson deconvolution. The main challenging tasks for deconvolution methods to superresolve images in OCT are the absence of accurate complex PSF and the inevitable ringing artifacts during the deconvolution.

In step 2, the deconvolved image $o(r)$ is further modulated by the phase masks of $\exp(i\varphi_m)$ in its respective Fourier domain $O(k_r)$. Through the forward and backward Fourier operation, a set of modulated images are averaged,

$$u(r) = \frac{1}{m} \sum_m \left| u_m(r) / \bar{u}_m(r) \right|$$

where $u_m(r) = F_r^{-1} \left[F_r(o(r)) \cdot \exp(i\varphi_{r,m}) \right]$ (4)

$\bar{u}_m(r)$ is the mean value of $u_m(r)$, \mathcal{F} denotes the 1-D Fourier transform, φ is normal random numbers with a mean of 0. RPM algorithm has two tuning parameters: the number of phase masks m , and the standard deviation of normal random numbers σ .

Results:

1. Demonstration of Deconv-RPM method on sub-resolution particles

To demonstrate the superresolving performance of the Deconv-RPM method, we imaged suspended sub-resolution particles in water. Detailed system construction of the spectral domain OCT (SD-OCT) has

been reported in our earlier work [24, 25]. In the proof-of-concept study, we first switched 2 Superluminescent Diodes (SLD1 and SLD3) off (Superlum Broadlighters cBLMD-T-850-HP, Ireland) to provide a light source with a center wavelength of 850 nm and a FWHM bandwidth of 55 nm, resulting in an axial resolution of 5.80 μm in air. The use of a self-made low numerical aperture objective lens allows a large confocal region of 177.84 μm at the expense of the transverse resolution was 9.81 μm in air. The polystyrene calibration spheres (CLB9, Sigma-Aldrich, Diameter 0.9 μm) are ideal as sub-resolution scatterers for characterizing the transverse and axial PSF of the OCT system.

The standard SD-OCT provides low-resolution images of the particles with both the coherent noise and the incoherent noise visible in the background (Fig. 2a). Using fixed Gaussian kernels derived from the theoretical PSF, Lucy-Richardson deconvolution improves both the transverse and the axial resolution but also gives rise to ringing artifacts (Fig. 2b) as expected. These artifacts are effectively suppressed by the random phase masks, while the improvement in resolutions by deconvolution is preserved (Fig. 2c). FWHM and Peak signal-to-noise ratio (PSNR) defined as $\text{PSNR} = 10\log_{10}(\text{MAX}^2(u_{img})/\text{Var}(n))$ [26] are used to compare the resolution and signal-to-noise level between the original image and the reconstructed image. In the confocal region, Deconv-RPM achieves 2.71 ± 0.46 times finer lateral resolution and 2.71 ± 0.51 times finer axial resolution than those of the standard SD-OCT (Figs. 2d and 2e). As shown in Fig. 2f, owing to an improvement of 13.4 ± 2.0 dB in PSNR, the image contrast is significantly enhanced in Deconv-RPM image.

2. Super-resolution imaging of nonkeratinized epithelial cells *in vivo*

To demonstrate the applicability of Deconv-RPM to static scatterers, we recorded the B-scans of human labial mucosa *in vivo* using μ -OCT (the system used to produce high-resolution images in Supplementary Information, A 30 KHz A-line rate allows for a B-scan rate of 1024 lines at 29.3 frames per second.). The IRB at the Nanyang Technological University (IRB 2016-1-015) approved the human study *in vivo*, in which written informed consent was obtained from participating subjects. Speckle noise is inherent in coherent imaging [27], which reduces contrast and makes it difficult to resolve boundaries between highly scattered structures in the tissue. Standard B-scan averaging (Spatial compounding) [28] was applied to both unprocessed OCT images and Deconv-RPM images for speckle reduction that the reduction of speckle noise is inversely proportional to \sqrt{N} ($N = 50$). However, there is an inherent trade-off between the speckle reduction and the resolution improvement: averaging B-scan comes at the expense of image resolution. It is obvious that the Deconv-RPM image (Fig. 3b) is much sharper than the conventional OCT image (Fig. 3a) and the deconvolved image (Supplementary Fig. 2) throughout the depths. Specifically, nonkeratinized epithelial cells seen as nucleocytoplasmic boundaries can be unambiguously discerned (Figs. 3c and 3d, pink arrowheads in green dashed-line box). Moreover, inside a blurred, noisy vessel in the deep tissue fine structures (pink arrowheads in orange dashed-line box), presumably red blood cells, can be clearly visualized by Deconv-RPM, illustrating the expected resolutions gain and the reduction of noise.

Figures 3g and 3h show the volume-rendered epithelium with both the unprocessed and the reconstructed data. 10 frames averaging of the *en-face* images shows the high scattering signals from the nucleocytoplasmic boundaries. Depths relative to the epithelium *in vivo* are shown in Supplementary Movie 1. For reference, histology from swine floor of mouth indicates details of anatomical structures such as cytoplasm and nuclei [29].

3. Resolution-enhanced imaging of moving blood cells imaging in vivo

To demonstrate the potential of Deconv-RPM in moving scatterers, we performed labial mucosa imaging of a human volunteer using μ -OCT (A 126 KHz A-line rate allows for a B-scan rate of 512 lines at 246.1 frames per second.). We scanned the same location on the mucosa multiple times consecutively that moving structures such as red blood cells could be found at each B-scan. Figure 4 presents capillary blood flow containing a mass of blood cells, where the flow direction is marked by red arrow. Figure 4c was created by manually segmenting the capillary region in Fig. 4a and then applying Deconv-RPM to Fig. 4b. For better comparison between images with and without Deconv-RPM, 3X close-up view (Figs. 4b' and 4c') on the regions marked in Figs. 4b and 4c showing the real-time feature of blood cells. A single-step discrete Fourier transform (DFT) algorithm [30] was used for alignment of the B-scans that the capillary region was registered. Details of the moving structures for super-resolution imaging in human labial mucosa *in vivo* are shown in Supplementary Movie 2. The results presented above show that our proposed method is capable of improving the resolution for moving structures using μ -OCT in a noninvasive and real-time manner.

Discussions:

Current deconvolution algorithms applied struggles in the presence of noise such as that in OCT images. To quantitatively evaluate the performance of Deconv-RPM, we implement 1-D simulations following the processing steps in Fig. 1. The second row in Fig. 5a shows the noisy image u_{img} generated by the convolution of ideal points (top row of Fig. 5a) and a complex Gaussian PSF (transverse) followed by adding Gaussian white noise n . We measured the FWHM and the PSNR of intensity profiles. The variance of normally distributed noise $\text{Var}(n)$ was determined by a reasonable PSNR value of 25 dB, specified by the PSNR of the conventional OCT image (Fig. 2a). Sub-optimal w for the initial PSF was set, which amounts to a 1.1-fold increase in optimal w_{opt} . Note, w_{opt} is the FWHM of the absolute values of the PSF. Tuning parameters m and σ were 10000 and 0.7 respectively. Apparent ringing artifacts can be seen in the unregularized deconvolved image (third row of Fig. 5a) while Deconv_RPM provides artifact-free images with a 2.5-fold improvement in resolution (bottom row of Fig. 5a, Fig. 5b). Image restoration by Deconv-RPM typically took from roughly 70 s for a 1000 pixels \times 100 pixels matrix, performing 10 iterations in step 1 and 10000 resamplings in step 2, on a 3.4 GHz Intel core i7-3770 processor with 8 GB memory.

Each resampling is independent that a GPU-based parallel computing design could significantly accelerate the computational speed.

We also evaluated the resilience of Deconv-RPM method, clarifying the contributions of the parameters w , σ and m to the resolution improvement and the PSNR enhancement. Figure 5c illustrates a slight decrease in resolution improvement when w is away from the optimal w_{opt} . Put in a different way, the PSF estimation has little impact on the performance. By varying the standard deviation σ , we find that there exists an optimal σ for both resolution improvement and the PSNR enhancement, once other parameters are set (Fig. 5d). Figure 5e shows the ceiling of the algorithm performance when m increases. Under different noise levels of the unprocessed image, shown in Fig. 5f, Deconv-RPM is rather robust to improve resolution, with a PSNR gain of more than 10 dB in the low PSNR scenarios (unprocessed images, PSNR below 32.5 dB). For the experimental results, the FWHM w was set as the estimate of spatial resolution and the number of iterations t for Lucy-Richardson deconvolution was chosen as 4–10; σ and m were chosen empirically to ensure the suppression of artifacts. The pixel size in both spatial and frequency domains should fulfill the Nyquist sampling criterion.

Although our approach is successful in recovering cellular and sub-cellular features of human labial mucosa *in vivo*, there is room for future development. Some of the weak signals along with the artifacts generated by deconvolution could be also suppressed in step 2 of our approach. Usually, OCT systems encounter limited depth-of-focus when employing a high numerical aperture in the sample arm. Deconv-RPM is compatible with numerical refocusing methods such as interferometric synthetic aperture microscopy [7], aperture synthesis [31] and subaperture correlation [32]. In practice, scatterers outside the confocal region could be refocused before the Deconv-RPM processing. Strictly speaking, Deconv-RPM should rely on the phase stability. Since the unstable phase fronts among axial scans do not greatly modify the backscattered intensity, Deconv-RPM is also robust to these errors as Lucy-Richardson deconvolution [13].

Conclusion:

The standard deconvolution, in concert with the numerical random phase masks, permitted artifact-free imaging with an approximate 2.7-fold resolutions improvement, which significantly exceeds the performance of these two methods separately. In conclusion, this method could be directly applied to the conventional OCT image without any system modification, opens up new perspectives to perform super-resolution imaging with potentially drastic noise reduction for finding out the specific sub-cellular structures in the turbid tissues. More broadly speaking, Deconv-RPM method can work on any other coherent or incoherent imaging modality suffered from severe noise artifacts to render a super resolution image.

Abbreviations

OCT

optical coherence tomography

RPM

random phase masks

PSF

point spread function

Deconv

deconvolution

1-D

one-dimensional

FWHM

full width at half-maximum

μ -OCT

micro-OCT

SLD

Superluminescent Diodes

PSNR

peak signal-to-noise ratio

DFT

discrete Fourier transform

Declarations

Ethical Approval and Consent to participate

The IRB at the Nanyang Technological University (IRB 2016-1-015) approved the human study *in vivo*, in which written informed consent was obtained from participating subjects.

Consent for publication

Not applicable.

Availability of data and materials

The data that support the findings of this study are available from the corresponding author on reasonable request.

Competing interests

The authors declare that they have no competing interests.

Funding

This research is supported by the Singapore Ministry of Health's National Medical Research Council under its Open Fund Individual Research Grant (MOH-OFIRG19may-0009), Ministry of Education Singapore under its Academic Research Fund Tier 1 (2018-T1-001-144) and its Academic Research Funding Tier 2 (MOE-T2EP30120-0001).

Authors' contributions

X.G. and L.L. conceived the study. X.G. developed the algorithm, conducted the proof-of-concept studies. X.G., S.C. and L.L. contributed to the *in vivo* imaging studies. X.G. and L.L. supervised the overall project and participated in writing the manuscript. The authors read and approved the final manuscript.

Corresponding author

Correspondence to Linbo Liu.

Xin Ge,¹ Si Chen,¹ Kan Lin,¹ Guangming Ni,³ En Bo,¹ Lulu Wang,¹ and Linbo Liu^{1,2*}

¹School of Electrical and Electronic Engineering, Nanyang Technological University, Singapore 639798, Republic of Singapore

²School of Chemical and Biomedical Engineering, Nanyang Technological University, Singapore 637459, Republic of Singapore

³School of Optoelectronic Science and Engineering, University of Electronic Science and Technology of China, Chengdu 610054, China

*Correspondence: liulinbo@ntu.edu.sg (L. L.)

Acknowledgements

Not applicable.

Authors' information

Affiliations

School of Electrical and Electronic Engineering, Nanyang Technological University, Singapore

Xin Ge, Si Chen, Kan Lin, En Bo, Lulu Wang & Linbo Liu

School of Chemical and Biomedical Engineering, Nanyang Technological University, Singapore

Guangming Ni

References

1. Liu L, Gardecki JA, Nadkarni SK, Toussaint JD, Yagi Y, Bouma BE, Tearney GJ. "Imaging the subcellular structure of human coronary atherosclerosis using micro-optical coherence tomography". *Nat Med*. 2011;17:1010.
2. Liu X, Chen S, Cui D, Yu X, Liu L. "Spectral estimation optical coherence tomography for axial super-resolution". *Opt Express*. 2015;23:26521–32.
3. Shemonski ND, South FA, Liu Y-Z, Adie SG, Carney PS, Boppart SA. "Computational high-resolution optical imaging of the living human retina". *Nat Photonics*. 2015;9:440.
4. Zhou KC, Qian R, Degan S, Farsiu S, Izatt JA. "Optical coherence refraction tomography " *Nature Photonics*. 2019;13:794–802.
5. Liba O, Lew MD, SoRelle ED, Dutta R, Sen D, Moshfeghi DM, Chu S, de la Zerda A. "Speckle-modulating optical coherence tomography in living mice and humans". *Nat Commun*. 2017;8:15845.
6. Ginner L, Kumar A, Fechtig D, Wurster LM, Salas M, Pircher M, Leitgeb RA. "Noniterative digital aberration correction for cellular resolution retinal optical coherence tomography in vivo". *Optica*. 2017;4:924–31.
7. Ralston TS, Marks DL, Carney PS, Boppart SA. "Interferometric Synth aperture microscopy " *Nat Phys*. 2007;3:129.
8. Hillmann D, Spahr H, Hain C, Sudkamp H, Franke G, Pfäffle C, Winter C, Hüttmann G. "Aberration-free volumetric high-speed imaging of in vivo retina". *Sci Rep*. 2016;6:35209.
9. Adie SG, Graf BW, Ahmad A, Carney PS, Boppart SA, "Computational adaptive optics for broadband optical interferometric tomography of biological tissue," *Proceedings of the National Academy of Sciences* **109**, 7175–7180 (2012).
10. Adie SG, Shemonski ND, Graf BW, Ahmad A, Scott Carney P, Boppart SA. "Guide-star-based computational adaptive optics for broadband interferometric tomography". *Appl Phys Lett*. 2012;101:221117.
11. Yu L, Rao B, Zhang J, Su J, Wang Q, Guo S, Chen Z. "Improved lateral resolution in optical coherence tomography by digital focusing using two-dimensional numerical diffraction method". *Opt Express*. 2007;15:7634–41.
12. Yasuno Y, Sugisaka J-i, Sando Y, Nakamura Y, Makita S, Itoh M, Yatagai T. "Non-iterative numerical method for laterally superresolving Fourier domain optical coherence tomography". *Opt Express*. 2006;14:1006–20.
13. Ralston TS, Marks DL, Kamalabadi F, Boppart SA. "Deconvolution methods for mitigation of transverse blurring in optical coherence tomography". *IEEE Trans Image Process*. 2005;14:1254–64.
14. Woolliams PD, Ferguson RA, Hart C, Grimwood A, Tomlins PH. "Spatially deconvolved optical coherence tomography " *Applied optics*. 2010;49:2014–21.
15. Liu G, Yousefi S, Zhi Z, Wang RK. "Automatic estimation of point-spread-function for deconvoluting out-of-focus optical coherence tomographic images using information entropy-based approach". *Opt Express*. 2011;19:18135–48.

16. Hojjatoleslami S, Avanaki M, Podoleanu AG. "Image quality improvement in optical coherence tomography using Lucy–Richardson deconvolution algorithm". *Appl Opt.* 2013;52:5663–70.
17. Liu Y, Liang Y, Mu G, Zhu X. "Deconvolution methods for image deblurring in optical coherence tomography". *JOSA A.* 2009;26:72–7.
18. Liu Y-Z, South FA, Xu Y, Carney PS, Boppart SA. "Computational optical coherence tomography". *Biomedical Opt express.* 2017;8:1549–74.
19. Bianco V, Paturzo M, Memmolo P, Finizio A, Ferraro P, Javidi B. "Random resampling masks: a non-Bayesian one-shot strategy for noise reduction in digital holography". *Opt Lett.* 2013;38:619–21.
20. Bianco V, Memmolo P, Paturzo M, Finizio A, Javidi B, Ferraro P. "Quasi noise-free digital holography " *Light: Science & Applications.* 2016;5:e16142.
21. Bianco V, Memmolo P, Leo M, Montresor S, Distante C, Paturzo M, Picart P, Javidi B, Ferraro P. "Strategies for reducing speckle noise in digital holography". *Light: Sci Appl.* 2018;7:1–16.
22. Van Kempen GM, Van Vliet LJ. "Background estimation in nonlinear image restoration " *JOSA A.* 2000;17:425–33.
23. Dey N, Blanc-Feraud L, Zimmer C, Roux P, Kam Z, Olivo-Marin JC, Zerubia J. "Richardson–Lucy algorithm with total variation regularization for 3D confocal microscope deconvolution". *Microsc Res Tech.* 2006;69:260–6.
24. Chen S, Ge X, Liu X, Ding Q, Wang N, Wang X, Chen S, Liang H, Deng Y, Xiong Q. "Understanding optical reflectance contrast for real-time characterization of epithelial precursor lesions" *Bioengineering & Translational Medicine,* e10137.
25. Ge X, Tang H, Wang X, Liu X, Chen S, Wang N, Ni G, Yu X, Chen S, Liang H, Bo E, Wang L, Braganza CS, Xu C, Rowe SM, Tearney GJ, Liu L. "Geometry-Dependent Spectroscopic Contrast in Deep Tissues " *iScience.* 2019;19:965–75.
26. Ozcan A, Bilenca A, Desjardins AE, Bouma BE, Tearney GJ. "Speckle reduction in optical coherence tomography images using digital filtering". *JOSA A.* 2007;24:1901–10.
27. Ma X, Anting W, Fenghua M, W. Shuimei. and M. Hai.
28. Bashkansky M, Reintjes J. "Statistics and reduction of speckle in optical coherence tomography". *Opt Lett.* 2000;25:545–7.
29. Chen S, Liu X, Wang N, Ding Q, Wang X, Ge X, Bo E, Yu X, Yu H, Xu C. "Contrast of nuclei in stratified squamous epithelium in optical coherence tomography images at 800 nm". *J Biophotonics.* 2019;12:e201900073.
30. Guizar-Sicairos M, Thurman ST, Fienup JR. "Efficient subpixel image registration algorithms " *Optics letters.* 2008;33:156–8.
31. Bo E, Luo Y, Chen S, Liu X, Wang N, Ge X, Wang X, Chen S, Chen S, Li J. "Depth-of-focus extension in optical coherence tomography via multiple aperture synthesis". *Optica.* 2017;4:701–6.
32. Kumar A, Drexler W, Leitgeb RA. "Subaperture correlation based digital adaptive optics for full field optical coherence tomography". *Opt Express.* 2013;21:10850–66.

Figures

Figure 1

See image above for figure legend

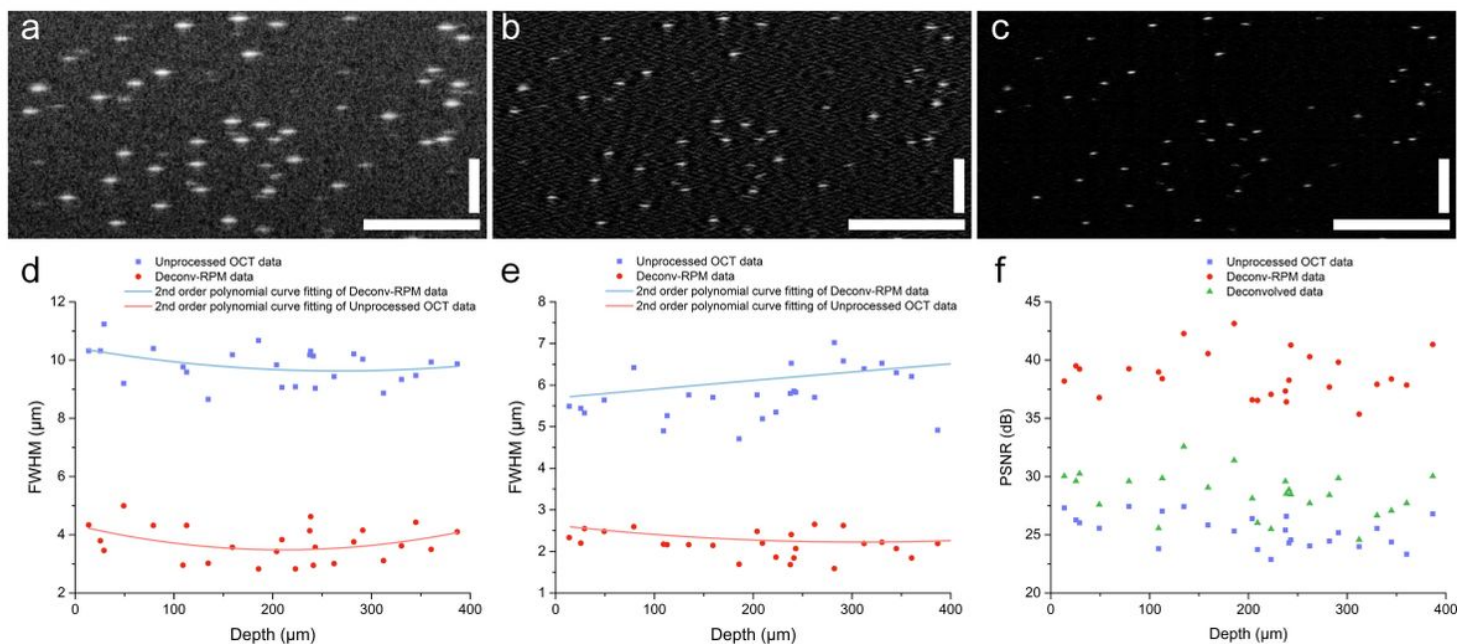


Figure 2

Recovery procedure of Deconv-RPM and demonstration of improved resolution and noise reduction.

Imaging of 0.9- μm -diameter particles acquired with standard OCT (a), processed with deconvolution only (b), and Deconv-RPM (c) on the logarithmic scale. Scale bars: 100 μm . OCT images before and after processing are presented at the same brightness and contrast levels. The FWHM of the transverse (d) and axial (e) profiles along the depth were shown in a (blue rectangle) and c (red circle). Data were fitted with a quadratic function in both cases. (f) Comparison of PSNR along the axial direction in a, b and c. The statistical analysis in (d-f) was performed on the linear-scale images. Also, see Supplementary Figure 1 for further quantification of the performance of the Deconv-RPM on the high-resolution image acquired with micro-OCT ($\mu\text{-OCT}$), and its comparison to the deconvolved-only image.

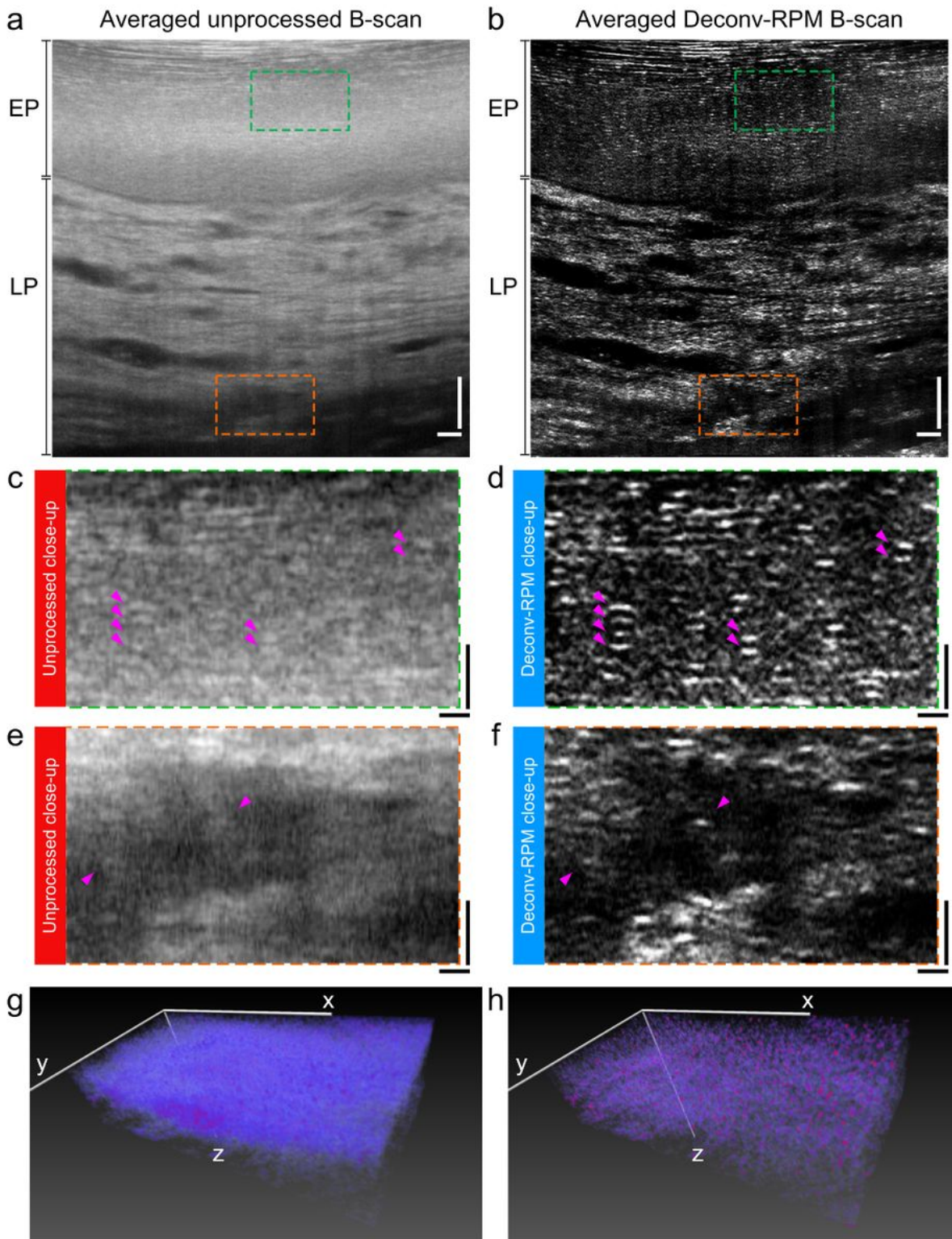


Figure 3

***In vivo* imaging of human labial mucosa.** (a, b) Conventional μ -OCT and Deconv-RPM imaging of human labial mucosa with 50 B-scan averages. EP: epithelium, LP: lamina propria. Scale bars, 50 μ m. (c, d) Zoomed view on high-scattering nucleocytoplasmic boundaries in the mucosal epithelium. Scale bars, 10 μ m. (e, f) Localized structures in the blood vessel are clearly visible in the magnified image (4X). Scale bars, 10 μ m. Brightness scaling of each image was set as the respective minimum and maximum to

prevent over-saturation. OCT images before and after processing are presented at the same brightness and contrast levels. (g, h) Reconstruction of Deconv-RPM data can be seen to significantly improve image quality over unprocessed OCT data. Ten frames were averaged in the *en-face* plane.

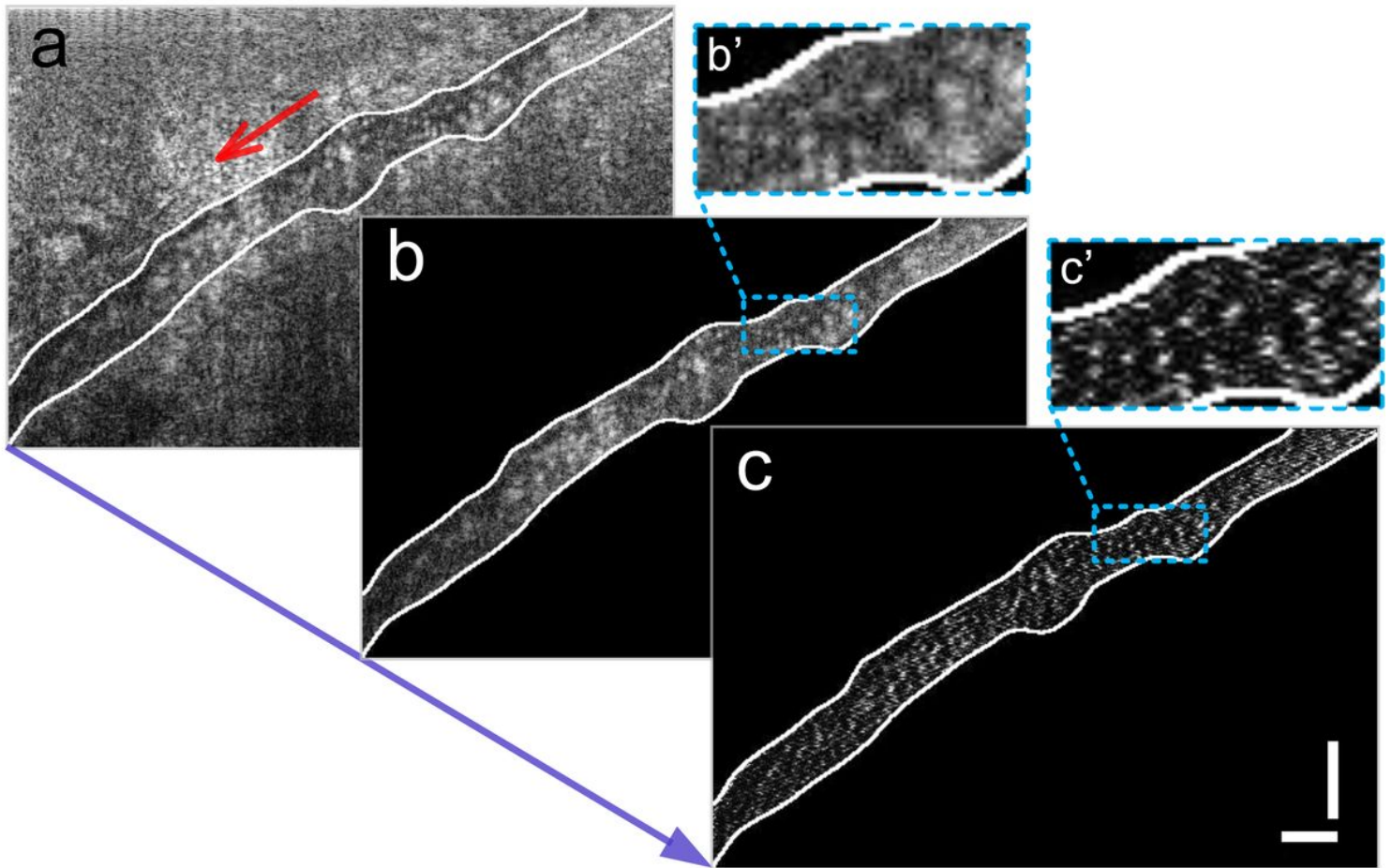


Figure 4

***In vivo* imaging of human capillary.** (a, b) Representative μ -OCT image and segmented capillary region of human labial mucosa. Scale bars, 50 μ m. (c) The corresponding Deconv-RPM image. (b', c') 3X zoomed view on blood cells in the capillary. OCT images before and after processing are presented at the same brightness and contrast levels.

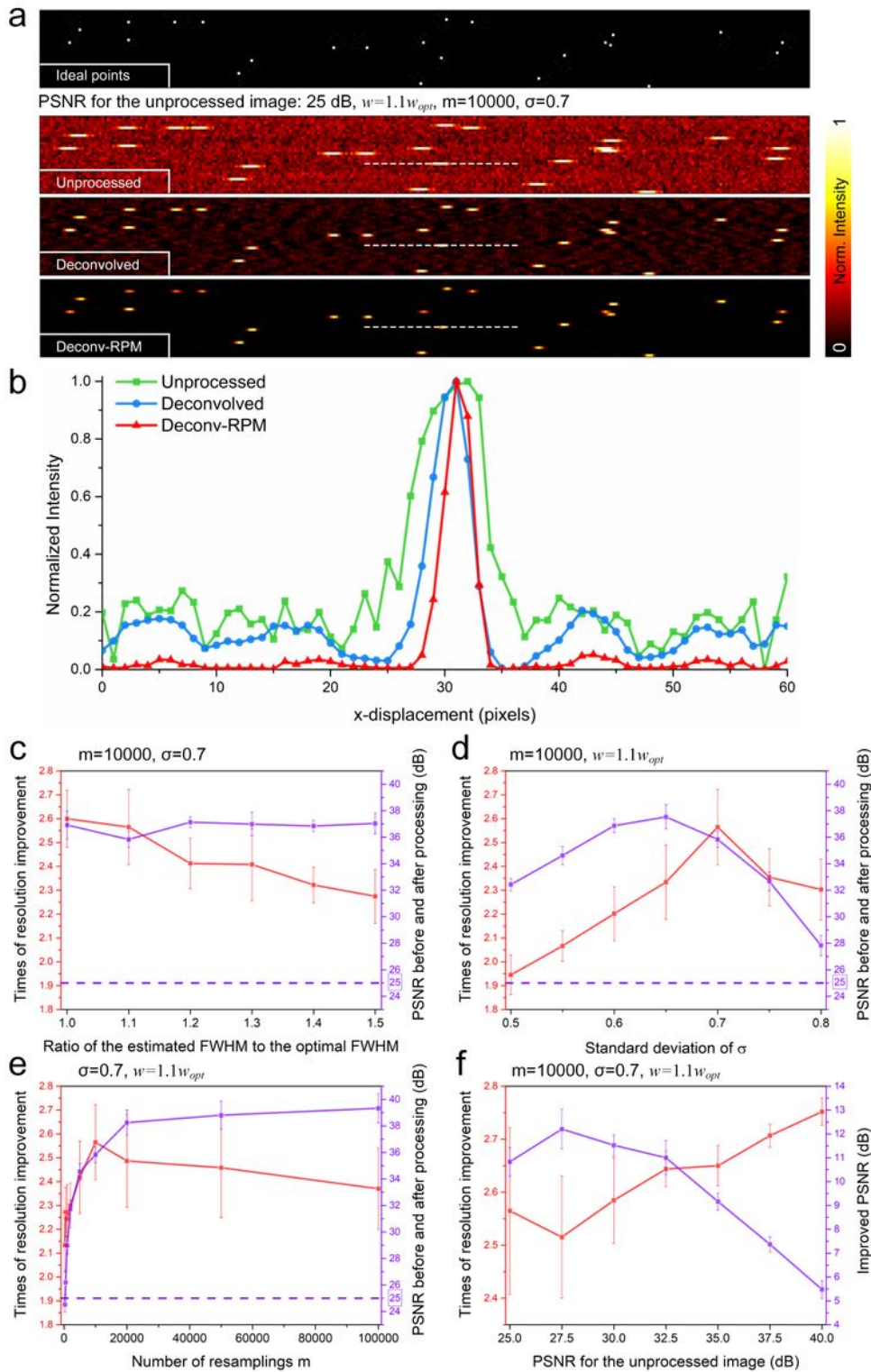


Figure 5

Effectiveness and resilience of Deconv-RPM method through 1D simulation and analysis. (a)

Representative simulation results on the logarithmic scale. Shown are the ground truth of spatial distribution of ideal points (top row), the unprocessed image of points blurred by a complex Gaussian function and additive Gaussian white noise, with PSNR = 25 dB (second row), the deconvolved image processed by Lucy-Richardson algorithm (third row), and the reconstructed image by two-step Deconv-

RPM (bottom row). (b) Transverse intensity profiles of the selected point indicated by the white dashes for a comparison. (c) Effects of real-valued FWHM estimation on resolution improvement and PSNR enhancement. (d) Times of resolution improvement and PSNR after processing as a function of the standard deviation of normal random numbers σ . Choice of σ value is depended on the balance of resolution improvement and PSNR enhancement. (e) Times of resolution improvement and PSNR after processing as a function of the number of resamplings m . $m = 10000$ is the ceiling of algorithm performance. PSNR for the unprocessed image in (a-e) is 25 dB. (f) Performance of restoration from low PSNR (25 dB) image to high PSNR (PSNR = 40 dB) image. Means and standard deviations in (c-f) are calculated by the repeated 10 simulations. Relative parameters are indicated in text. The number of iterations t is fixed to 10 in the deconvolution. Data analysis in (c-f) were calculated on the linear scale.

Supplementary Files

This is a list of supplementary files associated with this preprint. Click to download.

- [SupplementalText.pdf](#)
- [SupplementaryMovie1.avi](#)
- [SupplementaryMovie2.avi](#)